HHS Public Access

Author manuscript

Cancer Lett. Author manuscript; available in PMC 2024 April 01.

Published in final edited form as:

Cancer Lett. 2023 April 01; 558: 216094. doi:10.1016/j.canlet.2023.216094.

Lymphocyte antigen 6K signaling to aurora kinase promotes advancement of the cell cycle and the growth of cancer cells, which is inhibited by LY6K-NSC243928 interaction

Benson Chellakkan Selvanesan[a,b,*], **Sheelu Varghese**[a,b,*], **Justyna Andrys-Olek**[c], **Ricardo Hernandez Arriaza**[d], **Rahul Prakash**[d], **Purushottam Babu Tiwari**[e], **Daniel Hupalo**[b,f], **Yuriy Gusev**[e], **Megha Nitin Patel**[d], **Sara Contente**[a], **Miloslav Sanda**[g], **Aykut Uren**[e], **Matthew D. Wilkerson**[f,h], **Clifton Lee Dalgard**[f,h], **Linda S. Shimizu**[d], **Maksymilian Chruszcz**[d], **Tomasz Borowski**[c], **Geeta Upadhyay, Ph.D.**[a,e,h,†]

[a]Department of Pathology, Uniformed Services University of the Health Sciences, Bethesda, MD, USA.

[b]Henry M. Jackson Foundation, Bethesda, MD, USA.

[c]Jerzy Haber Institute of Catalysis and Surface Chemistry Polish Academy of Sciences, Cracow, Poland.

[d]Department of Chemistry and Biochemistry, University of South Carolina, Columbia, SC, USA.

[e]Department of Oncology, Georgetown University Medical Center, Washington, DC, USA.

[f]Department of Anatomy, Physiology, and Genetics, Uniformed Services University of the Health Sciences, Bethesda, MD, USA.

[g]Max Planck Institute for Heart and Lung Research, Ludwigstrasse, 43, 61231 Bad Nauheim, Germany.

[†]Correspondence: Geeta Upadhyay, Ph.D. geeta.upadhyay@usuhs.edu.

[*]Equally contributed

Author contribution:

Benson Chellakkan Selvanesan, Sheelu Varghese, Justyna Andrys-Olek, Ricardo Hernandez Arriaza, Rahul Prakash, Megha Nitin Patel, Purushottam Babu Tiwari, Daniel Hupalo, Yuriy Gusev, Sara Contente, Miloslav Sanda: Data curation; Formal analysis; Investigation; Methodology; Validation; Visualization; Writing - review & editing.

Aykut Uren, Matthew D. Wilkerson, Clifton Lee Dalgard: Resources; Supervision.

Linda S. Shimizu, Maksymilian Chruszcz, Funding acquisition; Supervision; Investigation; Writing - review & editing.

Tomasz Borowski: Methodology; Investigation; Writing - review & editing.

Geeta Upadhyay: Conceptualization; Data curation; Formal analysis; Methodology; Project administration; Resources; Software; Supervision; Validation; Visualization; Roles/Writing - original draft; Writing - review & editing.

Declaration of interests

The authors declare that they have no known competing financial interests or personal relationships that could have appeared to influence the work reported in this paper.

Disclaimer

The opinions expressed herein are those of the authors and are not necessarily representative of the official policies of the Uniformed Services University of the Health Sciences (USUHS), the Department of Defense (DOD), the United States Army/Navy/Air Force, the U.S. Government, or any other funding agencies.

Appendix A. Supplementary data

[h]John P. Murtha Cancer Center, Bethesda, MD, USA.

Abstract

Lymphocyte antigen 6K (LY6K) is a small GPI-linked protein that is normally expressed in testes. Increased expression of LY6K is significantly associated with poor survival outcomes in many solid cancers, including cancers from breast, ovary, gastrointestinal tract, head and neck, brain, bladder, and lung. LY6K is required for ERK-AKT and TGF-β pathways in cancer cells and is required for in vivo tumor growth. In this report, we describe a novel role for LY6K in mitosis and cytokinesis through aurora B kinase and its substrate histone H3 signaling axis. Further, we describe the structural basis of the molecular interaction of small molecule NSC243928 with LY6K protein and the disruption of LY6K-aurora B signaling in cell cycle progression due to LY6K-NSC243928 interaction. Overall, disruption of LY6K function via NSC243928 led to failed cytokinesis, multinucleated cells, DNA damage, senescence, and apoptosis of cancer cells. LY6K is not required for vital organ function, thus inhibition of LY6K signaling is an ideal therapeutic approach for hard-to-treat cancers that lack targeted therapy such as triple negative breast cancer.

Keywords

LY6K; NSC243928; Triple negative breast cancer; Aurora B

1. Introduction:

The lymphocyte antigen 6 (LY6) gene family proteins are present on human chromosomes 6, 8, 11, and 19, with corresponding genes in mouse syntenic regions (1). LY6K is one of the ten LY6 genes located on chromosome 8q24.3. LY6K is highly expressed in many cancers, including breast, ovarian, brain, head and neck, bladder, lung, and gastrointestinal tract (2,3). Increased LY6K expression is significantly associated with poor survival outcomes in these cancers, and it contributes to cancer cell growth via the ERK/AKT and TGF-β pathways in cancer cells in vitro and in vivo via a mechanism that is not fully understood (4,5). LY6K expression is normally confined to testes tissue and it is not required for vital organ function or for the maintenance of normal physiology. LY6K knockout male mice are infertile but otherwise normal. LY6K knockout female mice are fertile and phenotypically normal (6). Thus, LY6K is an attractive target for drug development because inhibition of this pathway may lead to tumor reduction without compromising essential organ functions. LY6K is a GPI-linked cell-surface glycoprotein that can be easily targeted by small molecules. Our previous work focused on the identification of small molecules that can bind to LY6K and induce cell death in LY6K-expressing cancer cells. We used the NCI small molecule library of more than 2500 compounds, which contained select anti-cancer compounds in a functional screen, to find an anti-cancer small molecule that selectively binds with LY6K. This work led to the discovery of NSC243928 as a binder of LY6K that promotes cancer cell death in a LY6K-dependent manner and does not bind to other LY6 family proteins (7).

Here, we report the structural basis of LY6K binding to NSC243928, and the molecular mechanism of LY6K action in the cancer cell cycle. We defined the 3D structure of LY6K protein and identified that phenylalanine 79 of LY6K is important for drug-

protein interactions using homology modeling and molecular dynamics simulations using I-TASSER, AlphaFold2, and Amber programs. Computational predictions of the LY6K-NSC243928 interaction were validated using wild-type and mutated LY6K proteins in a surface plasmon resonance assay. Furthermore, we used multiple cancer cell lines to demonstrate that NSC243928 inhibits cancer cell cycle progression and determine the mechanism by which NSC243928 functions in the disruption of LY6K induced cell cycle progression. We showed that LY6K is translocated to the nucleus and is associated with chromatin throughout mitosis. LY6K congregates at the mid body during cytokinesis. Treatment with NSC243928 reduced mitosis and cytokinesis. These effects were accompanied by a reduction in the phosphorylation of aurora B kinases and the phosphorylation of histone H3, a substrate of aurora B kinase. A functional consequence of NSC243928 induced disruption of LY6K signaling in the nucleus was observed as increased phosphorylation of histone H2A S139. Using LY6K knockout 4T1 cells, we observed that rescue with the wild-type LY6K plasmid, but not the phenylalanine 79 mutant, could restore the NSC243928 mediated inhibition of phosphorylation of aurora B and its substrate histone H3. These findings demonstrate a novel function of LY6K in mitosis and cytokinesis in cancer cells and demonstrate that LY6K binding small molecules may be used as pharmacological inhibitors of LY6K function in cancer cells. Furthermore, we showed that NSC243928 treatment induced DNA damage and apoptosis in two different mouse mammary tumor models in vivo. The findings presented in this report may lead to the development of safer and more effective targeted therapies for solid cancers.

2. MATERIALS AND METHODS

2.1 Purification of His tagged bacterial expression protein

Plasmids containing the sequences for N-terminal His-tagged mature LY6 proteins (wild type and mutant) were transformed into BL21 (DE3) *E. coli* via heat shock. Cells were grown and protein expression was induced with isopropyl β-D-1-thiogalactopyranoside (IPTG). After centrifugation, the cell pellet was collected and treated with urea buffer to obtain a protein lysate. Ni-NTA resin (Roche, Basel, Switzerland) was used in the batch purification method, and the protein was eluted using imidazole according to the manufacturer's instructions. Protein purity was assessed by SDS-PAGE on a 15% acrylamide gel.

2.2 I-TASSER molecular modeling of LY6K protein

A model of the LY6K mature protein (residues 18–138) was created using the I-TASSER server (8). I-TASSER creates models based on sequence similarity with ten homologous proteins with resolved 3D structures. In the case of LY6K, among the chosen templates, the most similar sequence was for the LYNX1 protein (NMR model; PDB:2L03) (9,10). The best predicted model yielded by the I-TASSER server protonation state (pH = 7.4) of titratable groups was resolved using propKa3.1, implemented on the PlayMolecule website (11, 12). Then, the model was placed in a virtual box with at least 10 Å distance between the model and the walls, the box was filled with TIP3P water molecules and neutralized with chloride ions. Thus, the entire system was subjected to energy minimization, heated from 0 to 300 K for 100 ps of NV dynamics with a Langevin thermostat, and then 1 ns (nano

second)-long MD equilibration at a constant pressure of 1 bar and constant temperature of 300 K. These preparatory steps were followed by 76 ns long “production” molecular dynamics simulation performed in isothermal-isobaric conditions (NPT, p = 1 bar, T = 300 K). The time step was set to 2 fs, and the geometries were saved every 5000 steps (every 10 ps). The SHAKE algorithm was applied to hydrogen atoms. Simulations were performed using the AMBER’s pmemd program (13). First, RMSD was calculated to visualize the stability of the overall protein structure and its individual components. Next, hierarchical agglomerative (HierAgglo) clustering of frames was performed to group them by their 3D structural similarity, based on RMSD for mainchain atoms, and to choose the most populated cluster and its centroid; the latter was used for further protein-ligand studies. *I-Tasser parameters:* I-TASSER uses three parameters to assess the quality of predicted structures. The first parameter is a TM-score to predict the similarity with the template; ideally, a TM-score over 0.5 is significant; second, a confidence score (C-score) assesses whether the model structure is assigned well and it falls in the range between −5 (non-reliable model) to 2 (model predicted with very good accuracy), and the third I-TASSER parameter is an estimated root mean square deviation (RMSD) between the model and the true structure; the higher the RMSD value, the worse the model.

2.3 AlphaFold2 molecular modeling of LY6K protein

AlphaFold2 is the second version of AlphaFold, an AI program created by DeepMind that predicts protein secondary structure using deep learning methods (14,15). Compared to I-TASSER, it also uses sequence similarities between homologous proteins (additional information about commonly occurring mutations is taken into account for enriching sequence alignments), in this case with the use of neural network architecture; however, information is passed to a different neural network that creates the 3D model. As an output, AF2 creates five models ranked according to the predicted local distance difference test (pLDDT) scale (0–100) that measures per-residue confidence. The models can be ranked from the best-ranked, a high 74.66 pLDDT value, to the worst a lower 72.14 pLDDT value for the LY6K model. The models differed mostly in the position of the N-terminus (amino acids 18–35). The best-ranked model underwent 100 ns of MD simulation at T = 300 K, p = 1 bar. The trajectories were then clustered into four clusters, and the structures of the cluster centroids were aligned to compare the differences and understand the motions of the model during MD simulation.

2.4 Synthesis and Purification of NSC243928

Small molecule NSC243928 was synthesized using a modified route based on a previous study (7), which facilitated purification to give >99% purity by LC (Supplementary Figure 1).

2.5 Docking studies of NSC243928 to LY6K

Once a reliable theoretical 3D representation of the mature form of LY6K was obtained, docking of NSC243928 to this model was performed using AutoDock Vina (16,17). Protein and ligand files used in docking were prepared using AutoDock Tools 1.5.6 version. This program was used to add partial charges and polar hydrogens to the protein. In the case of the ligand, in addition to partial charges and hydrogens, proper torsion parameters were also

set up following the software protocol. Blind docking was performed to target the entire model. To achieve this, a grid box of size 46 × 40 × 40 Å centered on the coordinates x = −0.078, y = 0.233, and z = −0.015 was created. The predicted binding affinities for all 27 poses were similar within the error of this program (16). Furthermore, AutoDock Vina has recently been shown to be the best at accurately predicting poses compared to estimating binding energy (17). Protein Data Bank, Partial Charge (Q), & Atom Type (T) (PDBQT) files of the protein and ligand were created using MGLTools (18). Three independent runs were performed, with the exhaustiveness parameter set at 32. Therefore, the overall binding of each pose was individually analyzed using the visualization program UCSF Chimera to select the best prediction (19). The two-dimensional diagram of LY6K and the initial binding pose of the drug were performed using ProteinPlus (20).

2.6 Molecular Dynamics (MD) simulation of NSC243928 and LY6K interaction

After docking the drug molecule to the MD-equilibrated LY6K I-TASSER model, 71 ns of MD simulation was performed for the complex, according to the above-mentioned methodology. This step requires prior parameterization of the ligand. Here, we applied GAFF2 parameters to the drug molecule with Restrained Electrostatic Potential method (RESP) charges obtained from fitting performed with the AmberTools RESP program (13). Snapshots from a 71 ns-long trajectory were clustered into two clusters. The clusters were then subjected to Molecular Mechanics Poisson-Boltzmann Surface Area (MMPBSA) energy calculations for the drug - protein complex. Computational alanine scanning mutagenesis (MMPBSA-CAS) studies were also performed to assess the role of amino acids in the binding pocket in protein-ligand interactions. Graphics were created using PyMol (21).

2.7 Surface plasmon resonance

A Biacore 4000 SPR instrument was used to record the SPR sensorgrams at 25°C with a CM5 sensor chip. Wild-type LY6K and mutant LY6K proteins were immobilized onto flow spots 1 or 5 in flow cells (FCs) 1 to 3 to a level of ~9000 Response Unit (RU) to 16000 RU. Standard amine coupling chemistry in the presence of 10 mM sodium acetate buffer (pH 4.0) was used to immobilize the proteins. PBS-P (20 mM phosphate buffer pH 7.4, 2.7 mM KCl, 137 mM NaCl, 0.05% surfactant P20) was used as the immobilization running buffer. Spot 3 of FCs 1–3 was used as a reference for spots 1 and 5. The reference spots had the same coupling chemistry as the active spots (spots 1 and 5), but no proteins were immobilized. Various concentrations of NSC243928 in PBS-P supplemented with 5% DMSO were injected into FCs at a flow rate of 30 μL/min. Each concentration of NSC243928 was injected in triplicate. The SPR sensorgrams were both reference (signals corresponding to the reference spots) and blank (PBS-P+5% only). The resulted sensorgrams corresponding to each LY6K protein were plotted using Biacore 4000 Evaluation Software version 1.1 for qualitative evaluation of NSC243928 binding to the LY6K proteins.

2.8 Cell culture, plasmids, drug treatment, transfection, and cell fractionation

4T1, E0771, BT549, Hs578T, HeLa, and 293T cells were obtained from ATCC and were cultured in Dulbecco’s modified DMEM medium (DMEM) supplemented with 10% fetal bovine serum (FBS), 2mM glutamine, non-essential amino acids, 1 mM sodium pyruvate,

100 U/mL pen/strep. Cells were plated at 50–60% confluency and allowed to attach. Cells were serum-starved for 8 hour and treated with drug overnight (18 h) or for indicated times in DMEM supplemented with 10% FBS. Cells were transfected using polyjet transfection reagent (SignaGen Inc. Frederick, MD, USA) according to the manufacturer's instructions. N-terminal His-tagged mature forms of human wild-type and mutant versions of LY6K (18–138 amino acid) were synthesized in the pET-24a vector (Epoch Life Science Inc., Missouri City, TX, USA) for protein expression in the bacterial system. Flag-tagged human LY6K was purchased from Origene, Rockville, MD, USA and was used for site-directed mutagenesis (Epoch Life Science Inc., Missouri City, TX, USA). Cell fractionation was performed using a subcellular protein fractionation kit for cultured cells (Thermo Scientific Inc., Waltham, MA, USA).

2.9 LY6K CRISPR knockout cells

pSpCas9(BB)-2A-GFP (PX458) (Addgene, Watertown, MA, USA) was used to clone the guide sequences for mouse LY6K. 4T1 cells were transfected with PX458-sg2-LY6K and PX458-sg3-LY6K, and GFP-expressing cells were flow-sorted. GFP-positive cells were grown using a clonal assay. The cells were then tested by PCR on genomic DNA to ascertain the genomic DNA deletion of the specified fragment. CRISPR cloning and cell generation were performed as described previously (22). The guide sequences for mouse LY6K gene ID 76486 were as follows: sg2-LY6K:1841-1860aa: GCTCGAATCCGTCCCAGTGC; sg3-LY6K:967-986aa: AGTGGCCTTGCTCGTAGTTC and were generated using the Integrated DNA Technologies, Coralville, IA, USA, webtool. Screening primers were generated using the NIH primer web tool. For the screening, we used the forward primer GGGCTGGCATCCAGACCAG and reverse primer AGGAATAGGAGCTGTCCAATCAAAGGTGA, which gave a 1158bp product in non-CRISPR cells while a 274bp band in CRISPR targeting with Sg2 and Sg3 LY6K guide sequences. We observed downregulation of LY6K protein in the CRISPR mutant cell clones (Supplementary Figure 2).

2.10 Generation of mouse monoclonal antibody for LY6K

A mouse monoclonal antibody against LY6K (CPTC-LY6K-3) was generated using a mature form of LY6K protein from amino acid 18–138. The antibody recognized 18 to 58 amino acids on the mature protein (Supplementary Figure 3). This work was supported in part by the National Cancer Institute's Clinical Proteomics Tumor Analysis Consortium (CPTAC)'s Antibody Characterization Program.

2.11 RNA sequencing and data analysis

Total RNA was isolated using the RNeasy kit and subjected to on-column DNA digestion (Qiagen Inc., Germantown, MD, USA). RNA was quantified using the Quant-IT RiboGreen RNA Reagent (Thermo Scientific, Waltham, MA, USA) and measured using a Spectramax Gemini XPS plate reader (Molecular Devices, San Jose, CA). RNA integrity was assessed using automated capillary electrophoresis on a fragment analyzer (Advanced Analytical Technologies Inc., Ankeny, IA, USA) with samples passing quality control for RIN values > 9. A total RNA input of 200 ng was used for library preparation using the Stranded Total RNA Library Preparation with Ribo-Zero Plus Kit (Illumina, San Diego, CA, USA).

Libraries were sequenced using a NovaSeq sequencer (Illumina, San Diego, CA, USA). Paired-end reads were aligned to the mouse reference genome (mm10) using MapSplice (version v2.2.2) with fusion transcript detection (23). Gene read counts against GENCODE (version 28) “basic” gene models were calculated using HTSeq (version 0.9.1) with the following parameters: -s reverse -t exon -m intersection-nonempty (24). Multimapping reads were discarded from analysis. Sample read counts per gene were normalized using EdgeR by log2 transformation with a minimum CPM of 0.5 (25). Missing values within the cohort were imputed using the median gene values. Differential expression was performed between each case and control pair using DESeq2 with a False Discovery Rate (FDR) cutoff of 0.1, and a minimum fold change of 2 (26). The most differentially expressed genes were further narrowed down using a fold-change cutoff of at least two and an FDR cutoff of 0.05. The intersection was used to identify genes that were commonly differentially expressed between all experiments and cell lines. The list of N=180 genes that were commonly differentially expressed was used for pathway enrichment analysis using Pathway Studio® Elsevier.

2.12 Cellular senescence

Senescence-associated β-galactosidase was detected using a staining kit after 48 h of drug treatment according to the manufacturer’s instructions (Cell Signaling Technologies Inc, Danvers, MA, USA). Images were taken using a Primovert Carl Zeiss Suzhou microscope, Suzhou, China, with a 20X objective and built-in camera.

2.13 Cell cycle analysis by flow cytometry

The cells were treated with different concentrations of the drug at different time points and after 24h, the cells were harvested using 0.25% trypsin and centrifuged at 3000×g for 5 min. The cells were then washed with PBS. After centrifugation, the cells were fixed in 100% ice-cold methanol overnight at −20°C. A fixed number of cells were taken and incubated in DAPI in PBS for 15 min at room temperature. Cell cycle analyses were performed using CytoFLEX (Beckman Coulter Inc., Brea, California), and the cell cycle data were analyzed using FlowJo software (FlowJo™ v10.7).

2.14 Cell cycle analysis by live cell imaging

HeLa cells were transduced with Incucyte® Cell Cycle Lentivirus Reagents (EF1α, Puro) (Sartorius Inc.). As quoted in manufacturer’s instructions –“The Cell Cycle Lentivirus Reagents are single-cassette, genetically encoded ubiquitination-based indicators that take advantage of cell cycle dependent changes in the expression patterns of Geminin and Cdt1”. This reagent links TagGFP2 and TagRFP (green/orange) to fragments of geminin and Cdt1, and the G1 and S/G2/M phases can be monitored in real time. Non-fluorescent cells represented the G1-M transition. The lentivirus was used as described in the manufacturer’s protocol. A lentivirus-transduced stable cell line was established using puromycin selection (1 μg/mL). Cells were serum-starved for cell cycle synchronization and then stimulated with complete serum medium with or without the drug. Cells were imaged in red green and phase channels for cell-by-cell analysis every four hours for the indicated time period using Incucyte® S3 equipment at 10X magnification and analyzed using Incucyte® software.

2.15 Western blotting and antibodies

Cells were lysed in RIPA buffer containing 1X protease inhibitor cocktail and phosphatase inhibitor, samples were pulse-sonicated and centrifuged, the supernatant was separated, and the protein concentrations were determined using a Bio-Rad protein assay kit. Equal quantities of protein were electrophoresed on 4–10% SDS polyacrylamide gels and then transferred onto PVDF membranes. Membranes were incubated with the indicated primary antibodies in Tris-buffered saline. After washing, membranes were incubated with HRP-conjugated anti-mouse IgG (1:3000) and Goat anti-rabbit IgG (1:3000). Protein bands were detected using a chemiluminescence system (ECL Kit, Thermo Scientific, Waltham, MA, USA), imaged, and quantified using the iBright 1500 imaging system (Invitrogen, Waltham, MA). For western blotting, primary antibodies for phospho-Histone H3 S10 (cat #53348), Histone H3 (cat# 4499), Phospho-Aurora A T288/Aurora B T232/Aurora C T198 (cat # 2914), Aurora B (cat # 3094), Cyclin E1 (cat # 20808), Cyclin B1 (cat # 12231), phospho-Histone H2A.X S139 (cat # 9718), Histone H2A (cat # 2578), Phospho-CHK1 S345 (cat # 2348), CHK1 (cat # 2360), cleaved caspase 3 D175 (cat # 9664), cleaved caspase 7 D198 (cat #8438), cleaved PARP D214 (cat #5625) from Cell Signaling Technologies Inc, Danvers, MA, USA. The α-tubulin (cat # T5168) was from Sigma Aldrich Inc, St. Louis, MO, USA. MCM4 (cat # 28317), Cyclin A (cat #sc 53230) antibodies were from Santa Cruz Biotechnology Inc, Dallas, Texas. DYKDDDDK Tag (Flag) (cat #TA50011) was obtained from OriGene, Rockville, MD, USA. A mouse monoclonal LY6K antibody (CPTC-LY6K-3) was raised against the mature form of LY6K protein (Antibody Characterization Program, Clinical Proteomics Tumor Analysis Consortium (CPTAC), National Cancer Institute, Bethesda, MD, USA), rabbit polyclonal LY6K antibody (cat # PA5-72689) was from Thermo Scientific, Waltham, MA, USA.

2.16 Immunofluorescence and confocal analysis

The cells were fixed in 4% paraformaldehyde and permeabilized using 0.5% Triton X-100 in PBS for 5 min. Cells were blocked in 3% BSA and stained with LY6K mouse monoclonal antibody generated against the mature peptide (18–138 amino acid) (CPTC-LY6K-3, (Antibody Characterization Program, Clinical Proteomics Tumor Analysis Consortium (CPTAC), National Cancer Institute, Bethesda, MD, USA) or Phospho-Aurora A T288/Aurora B T232/Aurora C T198 (cat # 2914) from Cell Signaling Technologies Inc, Danvers, MA, USA. A mouse monoclonal anti LY6K antibody (cat # NBP2-36764, Novus Biologicals Inc, Centennial CO, USA) was used additionally to confirm the LY6K labeling pattern. Goat anti-mouse Alexa Fluor Plus 488 secondary antibody (cat # A32723, Thermo Scientific, Waltham, MA, USA) or Goat anti-rabbit Alexa Fluor Plus 594 secondary antibody (cat # A32740, Thermo Scientific, Waltham, MA, USA) was used to visualize labeling. Imaging was performed using a Zeiss LSM700 confocal microscope. Super resolution confocal microscopy was performed using Aairyscan LSM980 with a 60x oil objective.

2.17 In vivo tumor treatment, tumor measurement and statistical analysis

Animal experiments were performed under an IACUC approved protocol at USUHS. The mammary tumor cell line 4T1 was injected subcutaneously into the mammary gland.

Tumors were established and treated with NSC243928 via the i. v. route or I.P. route at 50 mg/kg body weight. Tumor length and width were measured using Vernier calipers. Tumor volume was calculated using the formula (Width^2) × Length/2. To calculate the growth rate of the tumor, tumor volumes were converted to log values using the formula LOG10(tumor volume). The slope, which is the tumor growth rate per day, was calculated using (tumor volume series over days) (27). Statistical analysis was performed using an unpaired non-parametric Mann-Whitney test.

2.18 Immunohistochemistry

Tumors were dissected from the mice, immediately fixed with buffered formalin, and embedded in paraffin. Sections (5 μm) were cut and placed on slides and then deparaffinized at 60°C for 1 h, followed by xylene, an ethanol gradient (100%–70%), water, and PBS. The slides were then incubated for 20 min in 3% hydrogen peroxide, followed by boiling in citrate buffer for 20 min. Once the slides were cooled, washed, and blocked with 5% horse serum, the sections were incubated with primary antibodies, such as anti-cleaved caspase 3 (cat # 9664, Cell Signaling Technologies Inc, Danvers, MA, USA) at 1:100 dilution, and SignalStain Boost immunohistochemistry (IHC) detection reagent was used as a secondary antibody (Cell Signaling Technologies Inc, Danvers, MA, USA). Subsequently, the slides were incubated with 3,3'-diaminobenzidine (DAB) (Vector Laboratories Inc, Newark, CA, USA), counterstained with hematoxylin, dehydrated through an ethanol gradient (70%–100%) and xylene, and mounted with Permount. The slides were imaged using a Carl Zeiss Axio Vert A1 at 40X magnification.

3. Results

3.1 Determination of three-dimensional structure of LY6K protein and NSC243928-LY6K complex by molecular dynamics studies

An experimental structure of the LY6K protein is not yet available. Thus, homology modeling was used to predict the most probable 3D structure. According to I-TASSER parameters, the model of mature LY6K (LU domain aa18–138) had consistently better scores than the preprocessed forms - a N-terminal peptide (amino acids (aa) 1–17) and a C-terminal pro-peptide (aa 139–165). For the model of the mature protein, we performed a molecular dynamic (MD) simulation of 76 ns to further relax the predicted structure and gain information about protein flexibility. The LU-domain or mature form of the protein (18–138 aa), which consists of five anti-parallel β-strands in the middle of the protein, displayed a stable Root Mean Square Deviation (RMSD) profile and did not undergo any significant structural changes. Therefore, the overall RMSD value (~ 5 Å) is a result of the extensive movement of mobile loops and less ordered parts of the protein (Supplementary Figure 4A–B).

Molecular dynamics (MD) frames were clustered, and the centroid of the most populated cluster revealed a representative three-dimensional (3D) structure of the mature form of LY6K (Figure 1Ai). To ensure that this structure was indeed representative, we ran three additional independent 177ns long MD simulations, each starting from the same initial geometry. These three new trajectories were clustered, resulting in three new 3D structures

of LY6K (Figure 1Aii, 1Aiii, and 1Aiv). We found that these new 3D structures were highly similar to those obtained with the first MD simulation of 76 ns, as shown in Figure 1Ai. The high similarity of the protein mainchain conformation of these four structures strongly suggests that the structure chosen as a representative corresponds to a stable minimum. Hence, we used the 3D structure of LY6K to model its molecular interactions with NSC243928.

Docking studies were performed to create an initial computational model of binding between NSC243928 and LY6K. Three independent docking runs resulted in 27 different poses of the NSC243928-LY6K interaction with comparable binding affinities. We observed that out of 27 poses of the LY6K-NSC243928 interaction, 23 coincided at the same binding sites (Supplementary Figure 4C). The second step involved determining the most probable ligand orientation. Among these 23 poses, the drug was most buried within the protein when the acridinyl group was facing towards the inside of LY6K (Supplementary Figure 4D). A 2D representation of this binding pose showed the presence of three phenylalanine (F) residues at positions 52, 78, and 79, residing in this pocket (Supplementary Figure 4E). This observation suggests that the orientation of the drug may be stabilized by **π–π** stacking interactions. Using molecular dynamics simulations, we further investigated the computationally identified consensus-binding sites for NSC243928 to LY6K. These MD calculations showed that there are four F residues at positions 52, 75, 78, and 79 that are involved in the interaction of LY6K with NSC243928 (Figure 1B–C). MMPBSA calculation with alanine scanning mutagenesis (ASM) for the protein-ligand complex has revealed that point mutation F→A at positions 79 and 78 results in a noticeable energy increase, while the F→A mutation at position 52 and 75 has little or no effect on the binding. The energy of the WT complex was 20.3 kcal/mol, for the complex with 79 F→A, the energy was 24.8 kcal/mol (+4.5 kcal/mol); for 78 F→A 22.1 kcal/mol (+1.8 kcal/mol); for 52 F→A 21.0 kcal/mol (+0.7 kcal/mol); and for 75 F→A 20.0 (−0.3 kcal/mol). Independent structure analysis using AlphaFold2 (AF2) modeling of 3D structure of LY6K showed that the five best structure predictions generated by AF2 were identical in the beta-sheet region and very close to the I-TASSER model (Supplementary Figure 5A–E). Importantly, the *in silico* docking and MD simulations performed for the AF2 models showed an interaction of NSC243928 with F79 of LY6K, in agreement with I-TASSER modeling (Supplementary Figure 5F). Interestingly, F79 was one of the most highly conserved amino acids among the 21 species, including humans and mice (Supplementary Figure 6A). A 3D structural model of mouse LY6K generated by I-TASSER showed that F79 interacted with NSC243928 (Supplementary Figure 6B).

3.2 Phenylalanine 79 (F79) was a key interacting residue in LY6K to NSC243928.

To further confirm the involvement of these phenylalanine residues in LY6K-NSC243928 interactions, individual point mutations, phenylalanine (F) to alanine (A), were created in the mature form of poly-histidine (His)-tagged human LY6K. Bacterially expressed wild-type and F-to-A-mutated LY6K were purified using nickel columns for surface plasmon resonance (SPR) assays with highly purified NSC243928 (Figure 1D). We qualitatively evaluated the binding of NSC243928 to each LY6K protein immobilized on the SPR sensor surface, which showed that F79 is required for physical binding of NSC243928 to LY6K

(Figure 1E). This result supported the 3D modeled structure of the LY6K protein and its interaction with NSC243928, as generated by the I-TASSER program. Furthermore, we observed that an LY6K mouse monoclonal antibody binds to both WT LY6K and F79A LY6K with comparable affinities, suggesting that the F79 mutation does not destroy the ability of the protein to bind with its interacting partners.

3.3 Genome-wide RNA sequencing analysis identified changes in gene expression associated with chromatin remodeling and cell cycle

We previously observed that NSC243928 exposure of cancer cells results in cell death, with an IC50 range of 4 to 8 μM (7). To further understand the mechanism of cancer cell death, we assessed the transcriptional changes following drug treatment prior to cells experiencing widespread apoptosis. Thus, we chose to treat the mouse mammary cancer cell lines 4T1 and E0771 with a lower dose of drug i.e., 0.1 μM and 1.0 μM NSC243928 for 8 h, and then extracted RNA for a subsequent RNAseq analysis. Differential expression analysis identified a common set of 180 genes altered in both 4T1 and E0771 cell lines after exposure to NSC243928 at 0.1 μM and 1.0 μM concentrations (Supplementary Figure 7). A heatmap of the gene expression analysis of 180 genes showed significant agreement in three independent biological replicates in two different cell lines (Supplementary Figure 8). Pathway studio® analysis of 180 genes revealed a widespread alteration in chromatin-associated pathways, including chromatin remodeling via histone modification and DNA repair pathways, including double-strand breaks (Supplementary Table 1).

3.4 NSC243928 disrupted cell cycle progression

To determine the effect of NSC243928 on the cell cycle, 4T1 mouse mammary tumor cells were treated with increasing concentrations of NSC243928 for overnight (18 h) treatment. The control cells showed a typical 4T1 cell morphology, growing in a compact cluster of cells. The drug treated cells showed a distinct morphology of multinucleation and or enlarged nuclei (Figure 2A). Dot-plot analysis of cell size/number vs. DAPI labeling showed the expected cell cycle distribution in control untreated cells with 50% cells in G1, 25% in S-phase (2n nuclei), and 23.1% in G2/M, with very few polypoid cells (i.e., cells with ≥4n nuclei) (Figure 2Bi). In drug-treated cells, we observed a reduction in the G1 phase and disruption in the S to G2/M phase, with a dramatic increase in cells with ≥4n nuclei (Figure 2Bii). At a higher concentration of drugs, cells showed very few cells in the G1 and S-phase (2n nuclei), an abnormal G2/M phase, and a very high number of cells with ≥4n nuclei (Figure 2Biii). When these data were plotted using the Watson model in FlowJo software, we observed that both 4T1 and E0771 mouse cells showed higher numbers of cells in G2/M (yellow segment on the bar) and 4n state (purple segment on the bar) while the BT549, Hs578T, MDA-MB-231 human cancer cells showed high G2/M (yellow segment) and increased sub G1-apoptotic cell numbers (green segment on the bar) (Figure 2C–G, Supplementary Figure 9).

The effect of NSC243928 was visualized using live cell imaging in HeLa cells with the stable integration of cell cycle markers. HeLa cells are widely used to study cell cycle progression and express high levels of LY6K; thus, they are a relevant model to study the general effect of NSC243928 on cell cycle progression. This experiment showed that

NSC243928 treatment led to increased accumulation of cells in the S-G2-M phase in a concentration dependent manner (Figure 2H).

3.5 NSC243928 altered key cell cycle regulator protein expression

The mouse mammary tumor cell line 4T1 and human triple negative breast cancer lines BT549 and Hs578T were treated with increasing concentrations of NSC243928 overnight (18 h) and western blot analysis of cell cycle regulator proteins was performed. We observed that NSC243928 treatment led to reduced phosphorylation of His H3 at S10 (Figure 3A). The phosphorylation of histone H3 serine 10 (pHis H3 S10) is mediated by aurora kinases (28). We observed that NSC243928 treatment led to reduced phosphorylation of aurora B at T232. The phosphorylation for aurora A at T288 was not significantly changed. Phosphorylated aurora C at T198 was not evident in tested cell lines in control or treated cells (Figure 3A).

Among the protein expression changes associated with the cell cycle, NSC243928 treatment led to reduced cyclin D1 and increased cyclin A2 (Figure 3A). CyclinD1 is required for the G0-G1 and G1-S transition, and its levels remain high throughout the cell cycle in the S-G2-M phase. Cyclin A activates DNA replication in the S-phase, and levels of cyclin A peak during the S-G2 transition (29).

The mini-chromosome maintenance protein 4 (MCM4) is essential for the initiation of eukaryotic genome replication (30). The MCM4 protein levels were not affected by NSC243928 treatment (Figure 3A). This result suggests that NSC243928 does not affect MCM4 protein levels during the initiation of DNA synthesis. To confirm the effect of the drug in a time-dependent manner, HeLa cells were serum-starved for cell cycle synchronization and treated with 2.0 μM NSC243928 for the indicated time points. Western blot analysis showed that drug treatment led to reduced phosphorylation of histone H3 at S10, reduced phosphorylation of aurora B at T232, and increased cyclin A2 levels throughout the 24-hour time point (Supplementary Figure 10A).

3.6 NSC243928 inhibits cell cycle progression and induces DNA damage via interaction with LY6K

Reduced phosphorylation of aurora B kinase and its substrate Histone H3, alongside increased cyclin A and decreased cyclin D suggested a defective cell cycle progression leading to reduced cell division. Cells were serum starved overnight and then treated with complete medium with or without NSC243928. The control cells showed dividing nuclei and condensed nuclei, all together referred to as active nuclei but the drug treated cells did not exhibit normal nuclear division and very few active nuclei were observed (Figure 3B).

Defective nuclear division can trigger DNA damage, which can lead to cellular senescence and apoptosis (31). Indeed, treatment with NSC243928 increased senescence (Figure 3C). We then tested protein markers of DNA damage, repair, and apoptosis in NSC243928 treated cells. H2A.X is phosphorylated at S139, which marks the DNA damage site for the recruitment of cell death proteins(32). CHK1 is activated by phosphorylation at S345 following replicative stress (33). Poly (ADP-ribose) polymerase (PARP) is a protein that facilitates DNA repair and genomic stability and inhibits programmed cell death. PARP can

be inactivated and cleaved by activated caspase 3 and caspase 7 *in vivo*, leading to cell death (34). We observed that NSC243918 treatment led to increased phosphorylation of H2A.X at S139, increased phosphorylation of CHK1 at S345, increased activation of caspase-3 and caspase-7, and increased cleavage of PARP in 4T1 and BT549 cells (Figure 3D). Further, we examined the effect of drug treatment on the time course of HeLa cells exposed to 2 μM NSC243928 for the indicated times. Western blot analysis showed increased phosphorylation of histone H2A.X at S139, increased phosphorylation of CHK1 at S345, increased levels of cleaved caspase 3 and 7, and increased PARP cleavage in drug-treated HeLa cells (Supplementary Figure 10B).

Finally, to test if NSC243928 mediated inhibition of aurora B/histone phosphorylation and induction of phosphorylation of gamma H2A.X is dependent on LY6K interaction with NSC243928, LY6K CRISPR knockout 4T1 cells were generated using CRISPR method. We observed that LY6K knockout 4T1 cells have multinucleated morphology (see Supplementary Figure 2). NSC243928 treatment inhibited the phosphorylation of histone H3 and aurora B in LY6K-CRISPR cells transfected with wild-type LY6K, but not with F79A LY6K (Figure 3E).

3.7 LY6K is required for cell cycle progression and is associated with chromatin during mitosis

To determine whether LY6K translocates to the nucleus during the cell cycle, confocal microscopy using a mouse monoclonal antibody that recognizes the mature form of LY6K protein was performed. 4T1 cells were blocked in cell cycle using serum starvation overnight and then incubated with complete medium for 1 h to 24 h. Quantification of the total nuclear mean fluorescence intensity in the cells showed that LY6K was translocated to the nucleus within two hours of release and reached basal levels within 3 h (Supplementary Figure 11A). This observation suggested that LY6K plays a role in the nucleus during cell division. Therefore, we examined cells undergoing mitosis using Airyscan super-resolution confocal immunofluorescence. We observed that LY6K co-localized with active aurora kinase in the mitotic cells at the midzone and in cells undergoing cytokinesis at midbody in 4T1, BT549 and HeLa cells (Figure 4). LY6K co-localization to active aurora kinase was also confirmed using an additional mouse monoclonal LY6K antibody in HeLa cells (Supplementary Figure 12).

3.8 NSC243928 inhibits the nuclear translocation of LY6K and disrupts chromatin reorganization and cellular division.

Quantitative confocal microscopy demonstrated that LY6K accumulated in the nucleus and that treatment with NSC243928 inhibited nuclear LY6K accumulation at 2 h, whereas at 6 h, the levels in the control and treated cells were equal (Figure 5A, Supplementary Figure 11B). The cell fractionation assay showed that LY6K levels were reduced in chromatin-bound nuclear fractions, while LY6K levels were increased in the cytosolic fraction (Figure 5B). Confocal microscopy revealed that NSC243928 treatment led to disrupted chromatin organization and cytokinesis (Figure 5C). Cytokinesis is preceded by telophase, where the newly formed chromatids are still loose and less compact to ensure equal segregation of

the two sets of chromosomes in two new daughter cells, as seen in Figure 5; however, NSC243928 treatment led to chromosomes that were not well segregated (Figure 5C).

3.9 NSC243928 shows in vivo efficacy in reducing tumor growth, inducing DNA damage and apoptosis

4T1 mammary tumor syngeneic model was used to test the in vivo efficacy of NSC243928. Tumors were allowed to establish, and NSC243928 was administered three times, on post tumor cell inoculation day 11, on day 13 and on day 16. We observed that the treated group had a reduced tumor volume (Figure 6A). The growth rate (Figure 6B) and weight of excised tumors (Figure 6C) were significantly reduced in the treated group. Immunohistochemistry analysis showed extensive DNA damage in isograft tumors in the treated groups, as observed by increased gamma H2A.x S139 staining (Figure 6E) and significantly elevated levels of cleaved caspase 3 indicating apoptosis (Figure 6F).

NSC243928 treatment reduced tumor growth and induced DNA damage in the E0771 mammary tumor syngeneic mouse model immediately after two doses (Figure 7).

4. Discussion

LY6K is normally expressed in the testes, but is overexpressed in triple-negative breast cancer, bladder cancer, and ovarian cancer among other solid cancers (35–38). LY6K is required for in vivo tumor growth, and its increased expression is associated with poor survival outcomes (36–37, 40). Since LY6K protein is not required for vital organ function, it is an ideal target for antitumor treatments. We discovered that a small molecule, NSC243928, binds to LY6K and exerts anti-cancer properties. We focused on studies to determine the specifics of NSC243928 interaction with LY6K and the underlying mechanisms. In this study, we found that LY6K is translocated to the nucleus during mitosis, is associated with chromatin, and plays an important role in mitosis and cytokinesis. We further demonstrated that NSC243928 interacts with LY6K at amino acid F79, and that this interaction disrupts LY6K function in mitosis. These disruptions are manifested by reduced phosphorylation of aurora B and histone H3, and increased phosphorylation of histone H2A.X S139. Finally, these signaling pathways culminate in increased DNA damage that cannot be repaired, leading to PARP inactivation, senescence, and cell death by apoptosis.

Homology models of LY6K protein generated by means of the I-TASSER and AlphaFold 2 methods showed similar 3D structures of LY6K protein. Molecular dynamics simulations clearly indicated that NSC243928 binds to the protein at F79 with one of the hydrophobic residues interacting with the aromatic rings of the drug. Rescue experiments showed that F79 is indeed an important residue in the LY6K protein for drug interaction. We compared the environment of F79 with that of F52, which is exposed to the solvent, and that of F133, which is buried in the protein. The average solvent-accessible surface area for F79 was 41 $Å^2$, which is halfway between the values obtained for F52 (96 $Å^2$) and F133 (1$Å^2$) (Supplementary Figure 13). Future studies are required to determine how a conformational change due to NSC243928 binding to LY6K at F79 may affect the molecular interaction of LY6K with its partner protein. It is important to determine whether F79 is directly involved in the protein-protein interaction of LY6K, leading to its role as a cell cycle facilitator.

The mouse cells show increased G2/M accumulation (yellow segment in the bar) in addition to increased 4n (purple segment indicating polyploidy). Interestingly, these cells do not show increased subG1 (green segment indicating early cell death). The human cells show increased G2/M accumulation (yellow segment) and increased sub G1 (green segment), see Figure 2C. It is plausible that cell cycle network is somewhat diverse in mouse and human cancer cells. These results imply that drug treatment leads to cell death and/or polyploidy in mouse and human cancer cells. The western blot analysis in multiple cell lines revealed a loss of phosphorylation of aurora kinase B and its substrate histone H3 accompanied by accumulation of cyclin A, which suggested a G2/M phase arrest. This conclusion appears to be a consistent with reduced number of actively dividing nuclei, and with the increased number of cells residing in G2/M phase found by time lapse imaging of HeLa cells. It was also consistent with the increased DNA damage and CHK1 activation reported. LY6K knockout cells showed abnormal accumulation in G2 phase, increased number of fused and multinucleated cells mimicking the drug action.

Under normal circumstances in testicular germ cells, LY6K is present in the extracellular part of the cell membrane tethered to the outer leaflet of the plasma membrane in testicular germ cells, where it plays an important role in sperm migration (2,24). To understand the subcellular localization of LY6K and its role in cell cycle progression, LY6K immunofluorescence was performed using a mouse monoclonal antibody raised against the mature form of LY6K antibody. We observed that LY6K translocated to the nucleus and co-localized with aurora B during mitosis and during cytokinesis at the mid-body. NSC243928 treatment reduced the aurora kinase-LY6K interaction. NSC243928 also resulted in reduced phosphorylation of aurora kinase and its substrate Histone H3. NSC243928 induced inhibition of phosphorylation of aurora B kinase and inhibition of its substrate Histone H3 was rescued by wildtype LY6K but not by F79A mutated LY6K in LY6K CRISPR cells, confirming that NSC243928 effect on aurora B/histone H3 is linked with LY6K interaction of the drug at F79 at least partially.

Defects in cell cycle progression during mitosis and cytokinesis may result in DNA damage repair or can lead to the activation of senescence and apoptosis. We observed that NSC243928 treatment led to the inactivation of PARP proteins, in addition to the onset of senescence and activation of caspases. CHK1 proteins are direct effectors of DNA damage after replicative stress. We examined the phosphorylation of CHK1 following NSC243928 treatment and observed that CHK1 phosphorylation following drug treatment preceded the phosphorylation of H2A.X at Ser139, suggesting that CHK1 mediated phosphorylation of histone H2A may contribute to DNA damage via NSC243928-LY6K interaction. This suggests that NSC243928 could lead to DNA damage and eventually cancer cell death, as supported by in vivo observations of induced apoptosis and increased DNA damage due to NSC243928 treatment. Based on these findings, we present a novel field of study of LY6K biomarkers as cell cycle regulators. As LY6K expression is limited to the testes and is not necessary for vital organ function, there is strong potential for LY6K as a therapeutic target in many hard-to-treat cancers, such as triple-negative breast cancer and ovarian cancer, as well as any other cancer with the LY6K biomarker.

Supplementary Material

Refer to Web version on PubMed Central for supplementary material.

Acknowledgments

We appreciate the critical reading of the manuscript by Dr. Mary Lou Cutler, Professor of Pathology, Molecular and Cellular Biology, and Dr. Brian Schaeffer, Professor of Microbiology and Immunology, Uniformed Services University, Bethesda, MD.

Funding

1. National Institutes of Health (NIH), National Cancer Institute (NCI), R01CA227694 and R21CA256424.
2. NCI Antibody Characterization Program, Clinical Proteomics Tumor Analysis Consortium (CPTAC).
3. NIH shared instrument grant 1S10OD019982-01 (P30CA51008) Biacore Molecular Interaction Shared Resource (BMISR), Georgetown University.
4. VPR-NFP-74-9824, Department of Defense (DoD)Uniformed Services University of the Health Sciences (USUHS).
5. The Polish Grid Infrastructure, Cracow, Poland.
6. NIH P30CA51008 and 1S10OD019982-01 to Biacore Molecular Interaction Shared Resource (BMISR), Georgetown University.

References:

1. Loughner CL, Bruford EA, McAndrews MS, Delp EE, Swamynathan S, Swamynathan SK. Organization, evolution and functions of the human and mouse Ly6/uPAR family genes. Hum Genomics 2016;10:10 [PubMed: 27098205]
2. Upadhyay G Emerging Role of Novel Biomarkers of Ly6 Gene Family in Pan Cancer. Adv Exp Med Biol 2019;1164:47–61 [PubMed: 31576539]
3. Matsuda R, Enokida H, Chiyomaru T, Kikkawa N, Sugimoto T, Kawakami K, et al. LY6K is a novel molecular target in bladder cancer on basis of integrate genome-wide profiling. Br J Cancer 2011;104:376–86 [PubMed: 21063397]
4. Sastry NG, Wan X, Huang T, Alvarez AA, Pangeni RP, Song X, et al. LY6K promotes glioblastoma tumorigenicity via CAV-1-mediated ERK1/2 signaling enhancement. Neuro Oncol 2020;22:1315–26 [PubMed: 32055849]
5. Upadhyay G Emerging Role of Lymphocyte Antigen-6 Family of Genes in Cancer and Immune Cells. Front Immunol 2019;10:819 [PubMed: 31068932]
6. Fujihara Y, Okabe M, Ikawa M. GPI-anchored protein complex, LY6K/TEX101, is required for sperm migration into the oviduct and male fertility in mice. Biol Reprod 2014;90:60 [PubMed: 24501175]
7. Benti S, Tiwari PB, Goodlett DW, Daneshian L, Kern GB, Smith MD, et al. Small Molecule Binds with Lymphocyte Antigen 6K to Induce Cancer Cell Death. Cancers (Basel) 2020;12
8. Yang J, Yan R, Roy A, Xu D, Poisson J, Zhang Y. The I-TASSER Suite: protein structure and function prediction. Nat Methods 2015;12:7–8
9. Lyukmanova EN, Shenkarev ZO, Shulepko MA, Mineev KS, D'Hoedt D, Kasheverov IE, et al. NMR structure and action on nicotinic acetylcholine receptors of water-soluble domain of human LYNX1. J Biol Chem 2011;286:10618–27 [PubMed: 21252236]
10. The UniProt Consortium. 2019 UniProtKB - Q17RY6 (LY6K_HUMAN). <https://www.uniprot.org/uniprot/Q17RY6>.
11. Martínez-Rosell G, Giorgino T, De Fabritiis G. PlayMolecule ProteinPrepare: A Web Application for Protein Preparation for Molecular Dynamics Simulations. J Chem Inf Model 2017;57:1511–6 [PubMed: 28594549]

12. Olsson MH, Søndergaard CR, Rostkowski M, Jensen JH. PROPKA3: Consistent Treatment of Internal and Surface Residues in Empirical pKa Predictions. J Chem Theory Comput 2011;7:525–37 [PubMed: 26596171]
13. Case DA, Aktulga HM, Belfon K, Ben-Shalom IY, Brozell SR, Cerutti DS, et al. 2021 Amber 2021, University of California, San Francisco. <https://ambermd.org/CiteAmber.php>.
14. Jumper J, Evans R, Pritzel A, Green T, Figurnov M, Ronneberger O, et al. Highly accurate protein structure prediction with AlphaFold. Nature 2021;596:583–9 [PubMed: 34265844]
15. Varadi M, Anyango S, Deshpande M, Nair S, Natassia C, Yordanova G, et al. AlphaFold Protein Structure Database: massively expanding the structural coverage of protein-sequence space with high-accuracy models. Nucleic Acids Res 2022;50:D439–d44 [PubMed: 34791371]
16. Trott O, Olson AJ. AutoDock Vina: Improving the speed and accuracy of docking with a new scoring function, efficient optimization, and multithreading. Journal of Computational Chemistry 2010;31:455–61 [PubMed: 19499576]
17. Nguyen NT, Nguyen TH, Pham TNH, Huy NT, Bay MV, Pham MQ, et al. Autodock Vina Adopts More Accurate Binding Poses but Autodock4 Forms Better Binding Affinity. J Chem Inf Model 2020;60:204–11 [PubMed: 31887035]
18. Sanner MF. Python: a programming language for software integration and development. J Mol Graph Model 1999;17:57–61 [PubMed: 10660911]
19. Pettersen EF, Goddard TD, Huang CC, Couch GS, Greenblatt DM, Meng EC, et al. UCSF Chimera--a visualization system for exploratory research and analysis. J Comput Chem 2004;25:1605–12 [PubMed: 15264254]
20. Fährrolfes R, Bietz S, Flachsenberg F, Meyder A, Nittinger E, Otto T, et al. ProteinsPlus: a web portal for structure analysis of macromolecules. Nucleic Acids Res 2017;45:W337–w43 [PubMed: 28472372]
21. Schrödinger LD, W. 2020 PyMOL. <http://www.pymol.org/pymol>.
22. Ran FA, Hsu PD, Wright J, Agarwala V, Scott DA, Zhang F. Genome engineering using the CRISPR-Cas9 system. Nat Protoc 2013;8:2281–308 [PubMed: 24157548]
23. Wang K, Singh D, Zeng Z, Coleman SJ, Huang Y, Savich GL, et al. MapSplice: accurate mapping of RNA-seq reads for splice junction discovery. Nucleic Acids Res 2010;38:e178 [PubMed: 20802226]
24. Anders S, Pyl PT, Huber W. HTSeq--a Python framework to work with high-throughput sequencing data. Bioinformatics 2015;31:166–9 [PubMed: 25260700]
25. Robinson MD, McCarthy DJ, Smyth GK. edgeR: a Bioconductor package for differential expression analysis of digital gene expression data. Bioinformatics 2010;26:139–40 [PubMed: 19910308]
26. Love MI, Huber W, Anders S. Moderated estimation of fold change and dispersion for RNA-seq data with DESeq2. Genome Biol 2014;15:550 [PubMed: 25516281]
27. Hather G, Liu R, Bandi S, Mettetal J, Manfredi M, Shyu WC, et al. Growth rate analysis and efficient experimental design for tumor xenograft studies. Cancer Inform 2014;13:65–72 [PubMed: 25574127]
28. Hirota T, Lipp JJ, Toh BH, Peters JM. Histone H3 serine 10 phosphorylation by Aurora B causes HP1 dissociation from heterochromatin. Nature 2005;438:1176–80 [PubMed: 16222244]
29. Furuno N, den Elzen N, Pines J. Human cyclin A is required for mitosis until mid prophase. J Cell Biol 1999;147:295–306 [PubMed: 10525536]
30. Lei M, Tye BK. Initiating DNA synthesis: from recruiting to activating the MCM complex. J Cell Sci 2001;114:1447–54 [PubMed: 11282021]
31. Hayashi MT, Karlseder J. DNA damage associated with mitosis and cytokinesis failure. Oncogene 2013;32:4593–601 [PubMed: 23318447]
32. Yuan J, Adamski R, Chen J. Focus on histone variant H2AX: to be or not to be. FEBS Lett 2010;584:3717–24 [PubMed: 20493860]
33. Zhao H, Piwnica-Worms H. ATR-mediated checkpoint pathways regulate phosphorylation and activation of human Chk1. Mol Cell Biol 2001;21:4129–39 [PubMed: 11390642]

34. Boucher D, Blais V, Denault JB. Caspase-7 uses an exosite to promote poly(ADP ribose) polymerase 1 proteolysis. Proc Natl Acad Sci U S A 2012;109:5669–74 [PubMed: 22451931]

35. Maruyama M, Yoshitake H, Tsukamoto H, Takamori K, Araki Y. Molecular expression of Ly6k, a putative glycosylphosphatidyl-inositol-anchored membrane protein on the mouse testicular germ cells. Biochem Biophys Res Commun 2010;402:75–81 [PubMed: 20920470]

36. Luo L, McGarvey P, Madhavan S, Kumar R, Gusev Y, Upadhyay G. Distinct lymphocyte antigens 6 (Ly6) family members Ly6D, Ly6E, Ly6K and Ly6H drive tumorigenesis and clinical outcome. Oncotarget 2016;7(10):11165–93 [PubMed: 26862846]

37. Sastry NG, Wan X, Huang T, Alvarez AA, Pangeni RP, Song X, James CD, Horbinski CM, Brennan CW, Nakano I, Hu B, Cheng SY. LY6K promotes glioblastoma tumorigenicity via CAV-1-mediated ERK1/2 signaling enhancement. Neuro Oncol 2020;22(9):1315–1326. [PubMed: 32055849]

38. Kong HK, Park SJ, Kim YS, Kim KM, Lee HW, Kang HG, Woo YM, Park EY, Ko JY, Suzuki H, Chun KH, Song E, Jang KY, Park JH. Epigenetic activation of LY6K predicts the presence of metastasis and poor prognosis in breast carcinoma. Oncotarget 2016;7(34):55677–55689. [PubMed: 27494879]

39. Matsuda R, Enokida H, Chiyomaru T, Kikkawa N, Sugimoto T, Kawakami K, Tatarano S, Yoshino H, Toki K, Uchida Y, Kawahara K, Nishiyama K, Seki N, Nakagawa M. LY6K is a novel molecular target in bladder cancer on basis of integrate genome-wide profiling. Br J Cancer 2011;104(2):376–86. [PubMed: 21063397]

40. AlHossiny M, Luo L, Frazier WR, Steiner N, Gusev Y, Kallakury B, Glasgow E, Creswell K, Madhavan S, Kumar R, Upadhyay G.Ly6E/K Signaling to TGFβ Promotes Breast Cancer Progression, Immune Escape, and Drug Resistance. Cancer Res 2016;76(11):3376–86. [PubMed: 27197181]

- Discovery of a unique function for LY6K in mitosis and cytokinesis via aurora B kinase signaling in cancer cells.
- Structural underpinnings of the interaction between the inhibitor NSC243928 and the protein LY6K
- Mechanism of small molecule NSC243928 binding to LY6K and inhibition of cell cycle progression, resulting in failed cytokinesis, multinucleated cells, DNA damage, senescence, and cancer cell death.

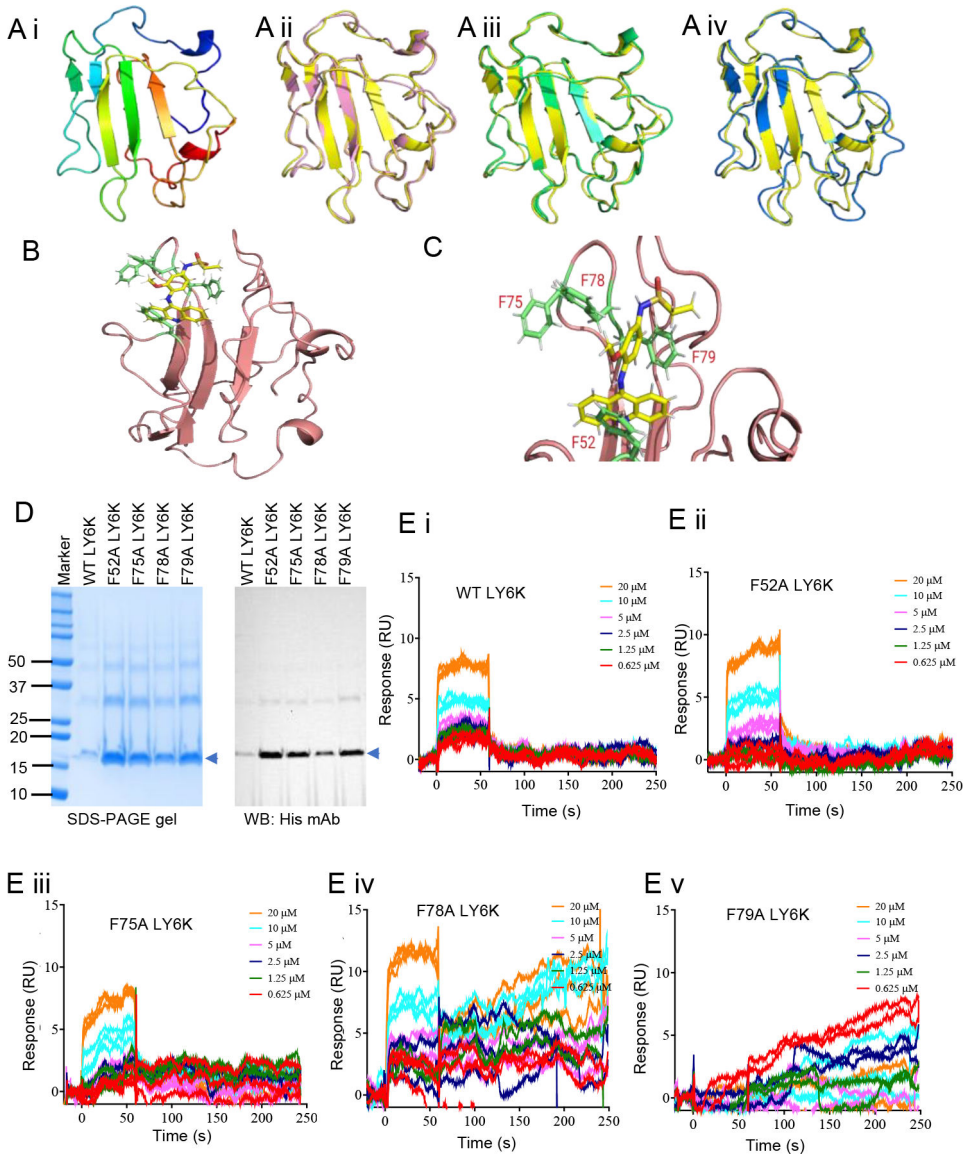

Figure 1:

(A) The basal model of mature LY6K protein selected from MD trajectory, presented in rainbow colors (i) N-terminus in blue and C-terminus in red. Comparison of the basal structure (yellow), presents structures of dominating clusters from three additional MD simulations, each 176 ns-long: (ii) colored pink, (iii) colored green and (iv) colored blue. **(B)** A 3D model of LY6K-NSC243928 in far view and in **(C)** closeup view - showed the LY6K-NSC243928 interaction involving 4 phenylalanines (F) at 52, 75, 78 and 79. **(D)** Indicated point mutations were created in His tagged human LY6K cloned in the pET24 vector. Recombinant protein was purified using Ni-NTA resin. The SDS-PAGE and western blot with anti-His mouse mAb confirmed the production of LY6K protein of expected size. **(E)** Surface plasmon resonance showed that (i) wildtype, (ii) F52A, (iii) F75A, and (iv) F78A LY6K retained binding to NSC243928, while (v) F79A LY6K did not show binding with NSC243928.

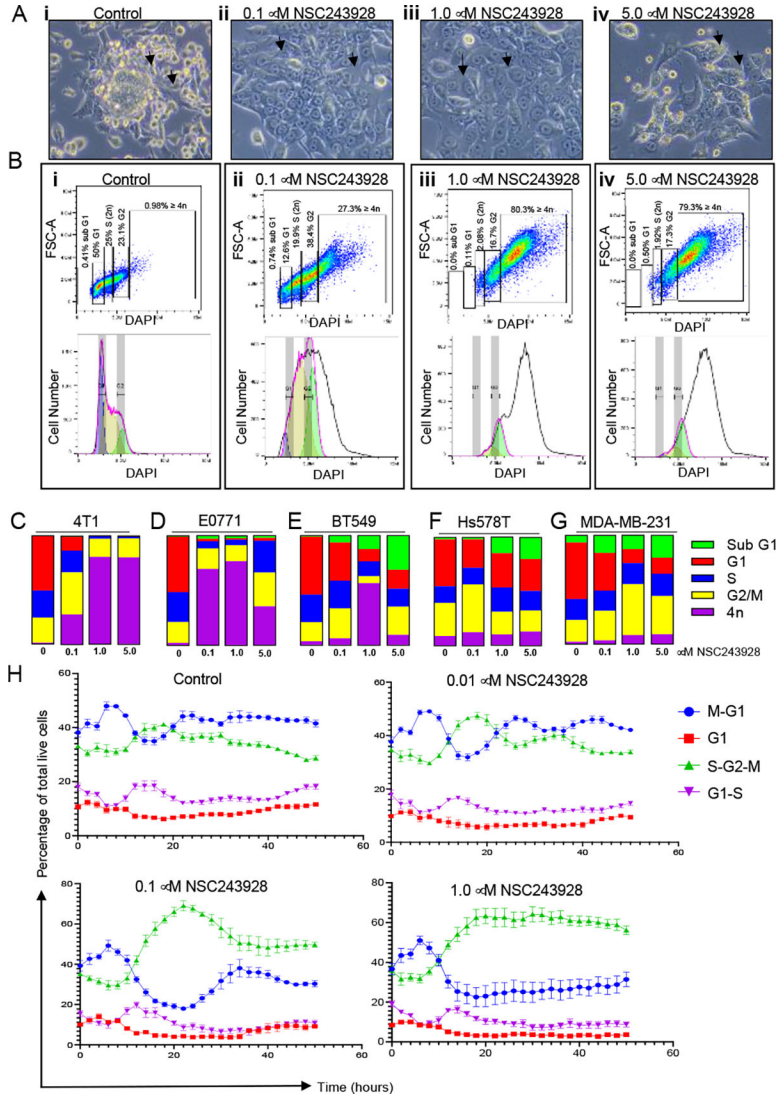

Figure 2:

NSC243928 induces morphological changes and G2/M arrest. Cells were serum starved for 8 hours and then treated with the indicated concentrations of the drug overnight (18 h). **(A)** Morphological observation indicated that (i) control cells grew in tight clusters, (ii) cells treated with a low concentration of NSC243928 (0.1 μM) did not exhibit gross toxicity but they were morphologically distinct with bigger nuclei, (iii) at an increased concentration of NSC243928 (1.0 μM) the cells displayed distinctly bigger nuclei, (iv) at the highest concentration of NSC243928 (5.0 μM) treatment cytotoxicity was observed and fewer cells were attached. **(B)** Cells were washed gently with PBS and collected by trypsinization, stained with DAPI and subjected to flow cytometry analysis. Data is shown in dot plots and in the Watson cell model to depict the various cell cycle stages in the bottom panel. We observed that (i) control cells show a normal distribution of subG1 (0.41%), G1 (50.1%), S (25%), G2/M (23.1%) cells, (ii) cells treated with a low concentration of NSC243928 (0.1 μM) show a slight increase in subG1 (0.74%), reduction in G1 (12.6%), slightly reduced S (19. 5%), increased G2/M phase (38.4%), dramatic increase in 4n and higher nuclei (27.3%),

(iii) at increased concentration of NSC243928 (1.0 μM) cells displayed G1 (0.11%), S (2.08%), G2 (16.7%), with a great increase in cell population with 4n and higher nuclei (80.3%), (iv) at the highest concentration of NSC243928 (5.0 μM), the pattern continues with the G1 (0.50%), S (1.92%), G2/M (17.3%), with increased 4n and higher (79.3%) cell numbers, suggesting that NSC243928 treated cells had high ploidy and they have difficulty in exiting the G2/M checkpoint. **(C-G)** The stacked bars were plotted to give the graphical analysis in multiple indicated cells lines of subG1, G1, S, G2/M cell population in the indicated cell lines at the indicated concentration of NSC243928 overnight (18 h) treatment. **(H)** HeLa cells stably transduced with Incucyte® cell cycle tracker dye were treated with indicated concentrations of NSC243928 and images were collected every four hours for 2 days. Automated live cell imaging and quantification was performed using Incucyte® S3 Live-Cell Analysis Systems.

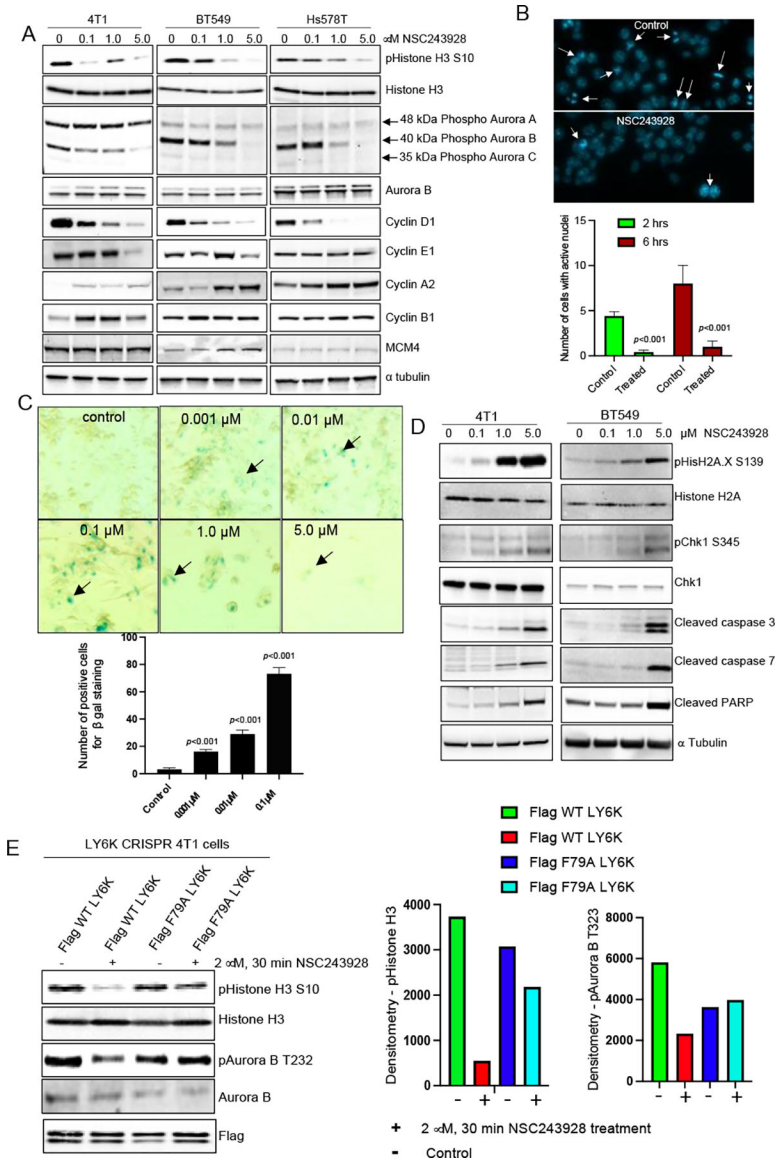

Figure 3:

NSC243928 inhibits cell cycle progression and induces apoptosis and cellular senescence. **(A)** Indicated cells lines were plated at 30% confluency, serum starved for 8 h and treated with the indicated concentration of drug in complete growth medium overnight (18 h). Cell lysates were prepared in RIPA buffer and western blot analysis was performed using indicated antibodies. **(B)** 4T1 cells were serum starved as above and then exposed to serum medium with or without drug for 2 h and 6 h. We observed that 2 μM NSC243928 treatment significantly eliminated the mitotic activity observed in control cells. Images are shown for 2 h time point. Bar graph below shows the number of mitotic/condensed DNA at 2 h and 6 h. *p* values are calculated compared to the control untreated. **(C)** Cells were plated at 20% confluency and treated with the indicated concentration of NSC243928 without serum starvation for 72 h and cellular staining for beta-galactosidase was performed, which showed increased cellular senescence at 0.1 μM NSC243928; black arrow for blue positive cells.

The 1.0 μM and 5.0 μM NSC243928 treatment for 48 h proved to be very toxic for cells as shown by the loss of attached cells. The bar graph below depicts the quantification. Five random fields were observed to count the beta-galactosidase positive blue cells. *p* values were calculated compared to the control untreated. **(D)** Indicated cell lines were plated at 30% confluency, serum starved for 8 h and treated with the indicated concentration of drug in complete growth medium overnight (18h). Cell lysates were prepared in RIPA buffer and western blot analysis was performed using indicated antibodies, which showed increased cleaved caspase 3, caspase 7 and cleaved PARP at increasing concentrations of NSC243928. **(E)** LY6K CRISPR knockout cells were serum starved as above and then treated with 2 μM NSC243928 for 30 min. Cell extracts were prepared in RIPA buffer for western blot analysis with indicated antibodies. The bar graph on right depicts the quantification of the western blot.

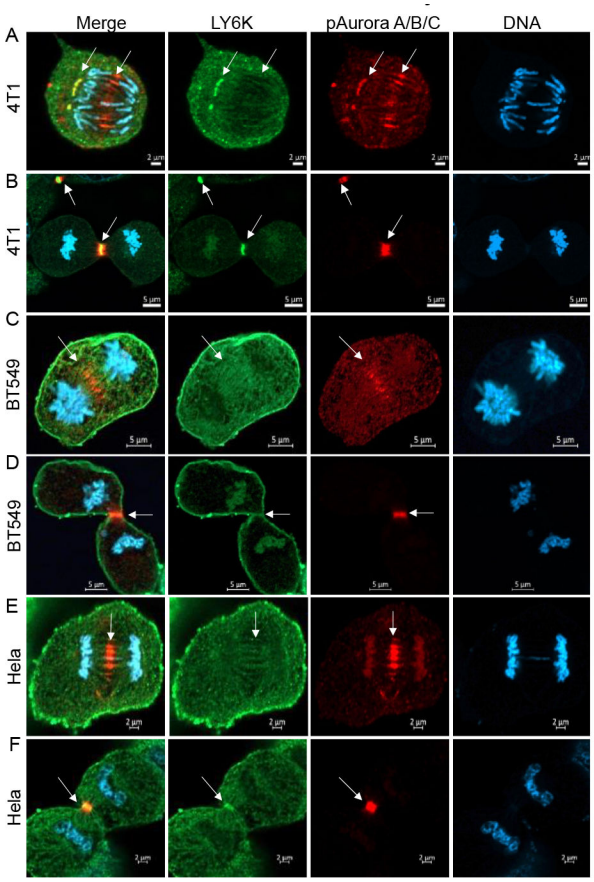

Figure 4:

LY6K co-localization with phosphorylated aurora kinase. Indicated cells were fixed in 4% paraformaldehyde and subjected to immunofluorescence using a mouse monoclonal antibody against LY6K and a rabbit polyclonal phosphorylated A/B/C antibody. The LY6K labeling was visualized using goat anti-mouse Alexa Fluor 488 (green). Phosphorylated Aurora A/B/C labeling was visualized with goat anti-rabbit Alexa Fluor 595 (red). The arrows indicate co-localization of LY6K and phosphorylated aurora proteins during **(A)** mitosis, and **(B)** cytokinesis in mouse mammary tumor 4T1 cells; **(C)** mitosis and **(D)** cytokinesis in human breast cancer BT549 cells and **(E)** mitosis and **(F)** cytokinesis in HeLa cells. DNA was labeled with DAPI (blue). Super-resolution confocal microscopy was done using Airyscan LSM980 with a 60X oil objective.

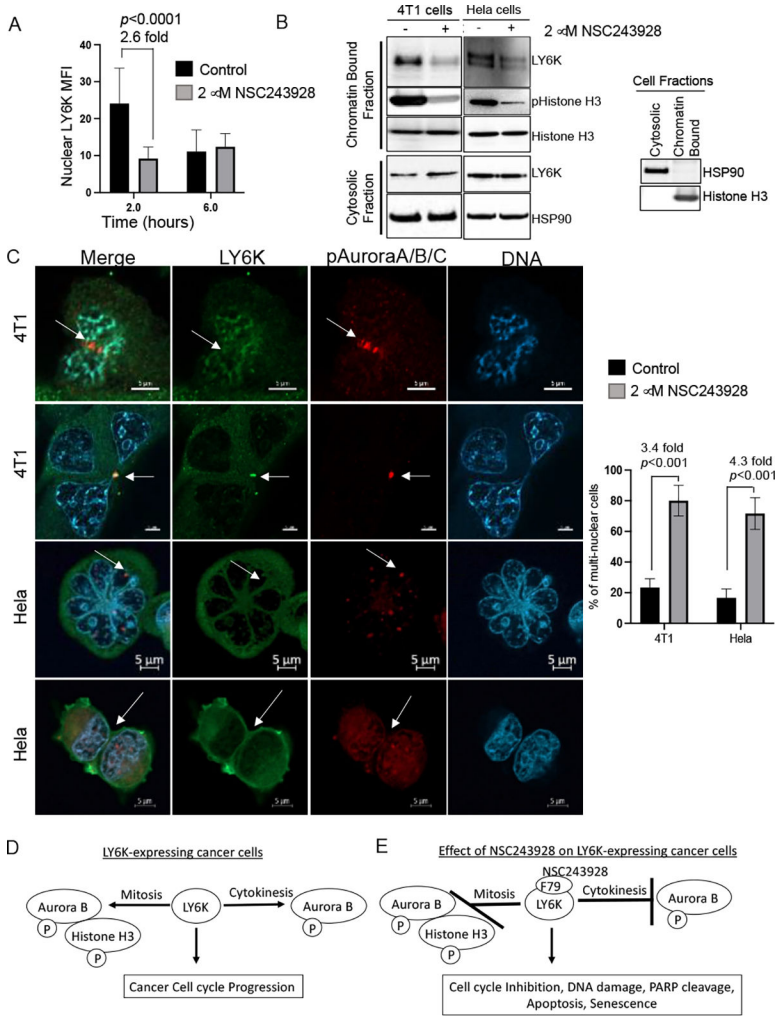

Figure 5:

NSC243928 inhibits nuclear LY6K function and localization. Indicated cells were serum starved for 8 hours and treated with complete medium with or without drug. **(A)** Quantification of nuclear LY6K signal as seen in confocal microscopy at 2 and 6 h with or without 2 µM NSC243928 treatment. **(B)** Cell fractionization was performed as described in methods with or without 2 µM NSC243928 treatment. Equal proteins were loaded for western blotting with indicated antibodies. The side panel shows the purity of cytosolic and chromatin bound fractions. **(C)** Immunofluorescence studies were performed in cells treated with 2 µM NSC243928. The drug treated cells showed binuclear or multinucleated cells with disrupted mitosis and cytokinesis. Interestingly, the co-localization of LY6K and aurora kinases was reduced as well. The quantification of multi-nuclear cells is shown in the bar graph. **(D)** Schematic representation LY6K-aurora B signaling in cancer cells to facilitate cell cycle progression **(E)** Schematic representation of NSC243928 induced disruption of LY6K-aurora B signaling leading to a halt in cell cycle progression leading to cell death.

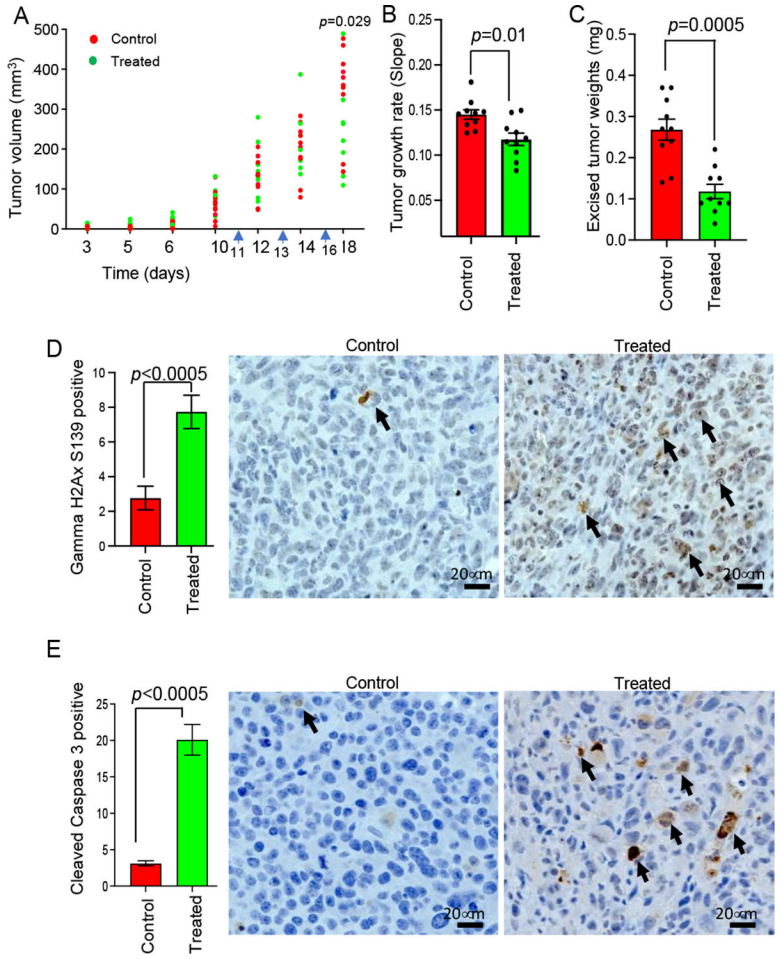

Figure 6.

In vivo effect of NSC243928 treatment. The control and treated groups had 10 mice each. All the mice were included in the analysis. **(A)** Tumor isografts in 4T1 mammary tumor model were grown to be larger than 50 mm^3. Mice were treated with NSC243928 at 50 mg/kg of body weight. First dose was delivered via i.v. on day 11 post cancer cell injection, second dose was delivered via i.p. on day 13 and third dose was delivered via i.v. on day 16. After three treatments, the treated group showed significant growth reduction compared to the control group. (**B)** The growth rate (volume per day) was significantly reduced in treated group compared to the control group. **(C)** Mice were euthanized and tumors were excised and weighed. Mice receiving drug had significantly lower tumor weight than controls. Tumor growth data (A-C) will be used elsewhere for the purposes not relevant to this work (manuscript in preparation). The excised tumors were formaldehyde-fixed and paraffin embedded. Tumor sections were stained with **(D)** gamma H2A.x S139 and **(E)** cleaved caspase-3 antibody. Three fields of view were monitored for positive cells (indicated by black arrows) from each section. The images were obtained with a 40X objective on Zeiss Axiovert microscope. Statistical analysis was performed with non-parametric Mann-Whitney Test using GraphPad Software. $p<0.05$ was considered significant.

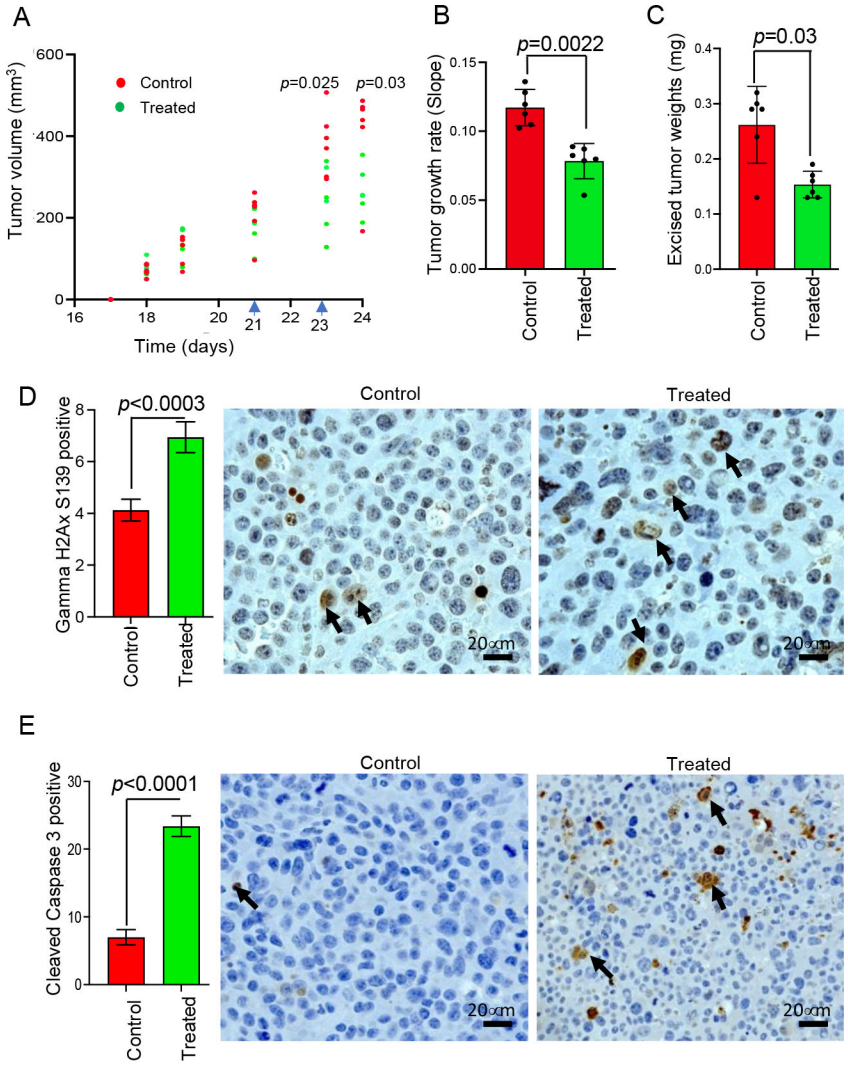

Figure 7.

In vivo effect of NSC243928 treatment. The control and treated groups had 5 mice each. All the mice were included in the analysis. **(A)** Tumor isografts in E0771 mammary tumor model were grown to be larger than 50 mm^3. Mice were treated with NSC243928 at 50 mg/kg of body weight. First dose was delivered via i.v. on day 21 post cancer cell injection, second dose was delivered via i.p. on day 23 post cancer cell injection. After two treatments, the treated group showed significant growth reduction compared to control group. (**B)** The growth rate (volume per day) was significantly reduced in treated group compared to the control group. **(C)** Mice were euthanized and tumors were excised and weighed. Mice receiving dug had significantly lower tumor weight than controls. Tumor growth data (A-C) will be used elsewhere for the purposes not relevant to this work (manuscript in preparation). The excised tumors were formaldehyde-fixed and paraffin embedded. Tumors were stained with **(D)** gamma H2A.x S139 and **(E)** cleaved caspase-3 antibody. Three field of view were monitored for positive cells (indicated by black arrows) from each section. The images were obtained using a 40X objective on Zeiss Axiovert microscope. Statistical analysis was

performed with non-parametric Mann-Whitney Test using GraphPad Software. A $p<0.05$ was considered significant.